Evolutionary divergence of anaphase spindle mechanics in nematode embryos constrained by antagonistic pulling and viscous forces

Dhruv Khatri[a], Thibault Brugière[b,c], Chaitanya A. Athale[a,*,†], and Marie Delattre[b,*,†]
[a]Division of Biology, IISER Pune, Pashan, Pune 411008, India; [b]Laboratory of Biology and Modeling of the Cell, Ecole Normale Supérieure de Lyon, CNRS, Inserm, UCBL, 69007 Lyon, France; [c]Centre de Recherche en Biologie Cellulaire de Montpellier (CRBM), CNRS, Université de Montpellier, 34090 Montpellier, France

ABSTRACT **Cellular functions such as cell division are remarkably conserved across phyla. However, the evolutionary principles of cellular organization that drive them are less well explored. Thus, an essential question remains: to what extent do cellular parameters evolve without altering the basic functions they sustain? Here we have observed six different nematode species for which the mitotic spindle is positioned asymmetrically during the first embryonic division. Whereas the *C. elegans* spindle undergoes oscillations during its displacement, the spindle elongates without oscillations in other species. We asked which evolutionary changes in biophysical parameters could explain differences in spindle motion while maintaining a constant output. Using laser microsurgery of the spindle, we revealed that all species are subjected to cortical pulling forces of varying magnitudes. Using a viscoelastic model to fit the recoil trajectories and with an independent measurement of cytoplasmic viscosity, we extracted the values of cytoplasmic drag, cortical pulling forces, and spindle elasticity for all species. We found large variations in cytoplasmic viscosity, whereas cortical pulling forces and elasticity were often more constrained. In agreement with previous simulations, we found that increased viscosity correlates with decreased oscillation speeds across species. However, the absence of oscillations in some species despite low viscosity can only be explained by smaller pulling forces. Consequently, we find that spindle mobility across the species analyzed here is characterized by a tradeoff between cytoplasmic viscosity and pulling forces normalized by the size of the embryo. Our work provides a framework for understanding mechanical constraints on evolutionary diversification of spindle mobility.**

Monitoring Editor
Alex Mogilner
New York University

Received: Nov 1, 2021
Revised: Feb 17, 2022
Accepted: Feb 23, 2022

INTRODUCTION

The mechanics of cytoskeleton and motors play a prominent role in cell division, transport and regulation, and influence of diffusion. This would also suggest that these properties governed by physical constants must scale to compensate for the diversity across evolution, for example, with cell size and shape differences. Potentially they may also constrain the evolutionary diversification of a widely conserved process such as cell division. Size scaling or allometry of intracellular components with cell size has been described. It lacks a simple explanation due to the diversity in mechanisms and missing principles regulating the size of intracellular organelles and structures (Reber and Goehring, 2015). The ubiquitous nature of the mitotic spindle has attracted similar approaches at size scaling through development and across evolution, since it involves the interplay of mechanical components of microtubules (MTs), motors, chromosomes, and regulators across species. Some recent work has proposed MT nucleation as a mechanism that determines spindle size scaling in development (Rieckhoff *et al*., 2020) that could provide a mechanism for the linear scaling of spindle and cell sizes during

This article was published online ahead of print in MBoC in Press (http://www.molbiolcell.org/cgi/doi/10.1091/mbc.E21-10-0532) on March 2, 2022.

†These authors contributed equally to this work.

Competing interests: The authors declare no competing interests.

*Address correspondence to: Chaitanya A. Athale (cathale@iiserpune.ac.in); Marie Delattre (marie.delattre@ens-lyon.fr).

Abbreviations used: A/P, antero/posterior; ATP, adenosine tri phosphate; DIC, differential interferential contrast; µm/s, micrometer per second; MSD, mean square displacement; MT, microtubule; NA, numerical aperture; Pa.s, Pascal second; pN, picoNewton; SD, standard deviation; SEM, standard error of the mean.

embryogenesis across species (Crowder *et al.*, 2015; Farhadifar *et al.*, 2015). However, understanding the evolutionary scaling of dynamical properties of spindles—their mobility, asymmetry, and motion—is expected to be more complex, due to the time-dependent nature of the process. Large changes in cellular properties may also be possible as long as the phenotypes under selection—output phenotypes—are not modified. These nonadaptive changes, or cryptic changes, help delineate the flexibility of biological mechanisms and their constraints (Lynch, 2007). To what extent physical properties can evolve without constraints on phenotypic variation remains to be explored.

In an attempt to address this, we previously characterized the first embryonic cell division in 40 species of nematodes closely related to *Caenorhabditis elegans* (Valfort *et al.*, 2018). In all these species, similarly to what has been described for *C. elegans*, an anterior/posterior (A/P) polarity axis is already established at the time of the first cell division (Delattre and Goehring, 2021). One manifestation of this polarity is the asymmetric displacement of the mitotic spindle during the first anaphase, from a central to a posterior position. Consequently, the division generates two daughter cells of unequal size and of unequal fate. We found the movements of the spindle during its displacement are very different from one species to the other, suggesting cryptic changes in the cellular parameters that govern spindle motion.

In *C. elegans* single-celled embryos, the spindle is initially centrally located. Asymmetric cortical pulling forces are responsible for its posterior displacement during anaphase. The entire spindle is first slightly shifted to the posterior in metaphase and early anaphase (Labbé *et al.*, 2004; Oegema *et al.*, 2001). Next, the posterior centrosome displaces faster and to a greater extent than the anterior centrosome during anaphase, generating asymmetric elongation (Grill *et al.*, 2001). Laser ablation of the central spindle at the onset of anaphase resulted in both centrosomes accelerating toward the cell poles, with the posterior centrosome velocity greater than the anterior, demonstrating that opposing and asymmetric pulling forces act on astral MTs to displace the centrosomes (Grill *et al.*, 2001). These movements result from the activity of a conserved dynein-containing protein complex anchored at the cortex (Kotak, 2019). During spindle displacement, the anterior and posterior centrosomes also oscillate back and forth along the transverse axis, in a manner that mimics anti-phase oscillations (offset by half a wavelength). These stereotypical movements, with reproducible build-up and die-down phases and specific frequency and amplitude, are referred to as spindle oscillations. Upon mild inactivation of the dynein-containing complex, spindle oscillations are abolished, yet the cell divides asymmetrically (Pecreaux *et al.*, 2006). Hence, although not essential, spindle oscillations have been the subject of considerable research because they serve as a readout of the collective mechanics, as summarized in a theoretical model of spindle oscillations (Grill *et al.*, 2005). A more recent model of spindle oscillation mechanics suggests an additional role for cell size in modulating spindle oscillations (Jiang, 2015). Such collective mechanics resulting in spatial oscillations or instabilities is seen in multiple models of MT motor systems such as a multiaster system with cortical dynein and dynamic instability (Khetan and Athale, 2020). *C. elegans* spindle oscillations were predicted by a model to be driven by cortical motors, and astral MT attachments predict that oscillations emerge above a threshold of active forces (Pecreaux *et al.*, 2006). At the same time, Kozlowski *et al.* (2007) predicted that a low cytoplasmic viscosity was also required for oscillations with speeds greater than 0.2 μm/s, since higher viscosities resulted in a strong damping force opposing the motor-forces. Indeed *C. elegans* spindle oscillations have also been quantitatively reproduced by models of the mechanics of MT motors (Grill *et al.*, 2003, 2005; Kozlowski *et al.*, 2007). Cortical force generators (dynein-containing complexes) pull from each side of the cortex (upper and lower), which should leave the centrosome in a stable central position (Ma *et al.*, 2014). In metaphase spindles of *C. elegans* embryos, these forces maintaining the central position have recently been estimated by fitting a viscoelastic model to perturbation–relaxation experiments on intact spindles (Garzon-Coral *et al.*, 2016), and these are likely to be comparable to forces acting at anaphase. The transverse displacement of the centrosomes is explained in the model by a positive feedback mechanism as a result of which a slight displacement of the centrosome toward the upper cortex, for instance, is amplified because pulling forces increase as the centrosome comes closer to the cortex, a scenario that results from the load per motor decreasing with decreasing distance to the centrosome (Pecreaux *et al.*, 2006). The restoring force acting to recenter the centrosome could be generated by astral MTs pushing on the cortex as they polymerize (Kozlowski *et al.*, 2007), or by the buckling of these MTs, extending laterally to the oscillation axis (Pecreaux *et al.*, 2006). The tug of war between these pulling and restoring forces generates the oscillations. Pulling forces must also counterbalance the damping force generated by the viscous cytoplasm to launch the oscillations. Spindle motion is thus caused by the complex interplay between the driving mechanical forces and the material properties of the cell and of the spindle.

Our quantification of spindle motion across nematode species revealed that spindle transverse oscillations are restricted to *Caenorhabditis* species (Valfort *et al.*, 2018). In *C. monodelphis*, which is the most basal *Caenorhabditis* species, and in all species outside of this genus, the anaphase spindle is asymmetrically displaced without any transverse oscillations. Here, we asked which cellular parameter change accounts for this absence of oscillations. A simple hypothesis is that the viscosity of the cytoplasm could give rise to these differences, based on predictions from simulations of *C. elegans* spindle-oscillatory mechanics (Kozlowski *et al.*, 2007). However, these predictions remain to be tested experimentally, since altering cellular viscosity without affecting cell physiology is technically challenging. Alternatively, if the net pulling forces are reduced, we also expect the loss of oscillations. Across species, spindle oscillation buildup may be hindered by an increase in cytoplasmic viscosity or by a reduction in cortical forces arising from gene expression changes, reduced cortical localization, or other parameter change such as cell size.

In this study, we address the question of how many biophysical features explain the diversity of spindle motion observed between species. In doing so, we specifically asked which combination of parameters have been retained over the course of evolution as good solutions to sustain asymmetric cell division. We chose six representative species and examined the recoil kinetics of the spindles to examine the role of pulling forces. To estimate these, we measure the cytoplasmic viscosity and its variability between species. We use a viscoelastic model to measure the cortical pulling forces responsible for spindle motion in all species. We then ask which changes in the force, viscosity and recoil kinetics across species correlate with spindle motion kinetics. Our evolutionary approach helps challenge the current theoretical models of spindle motion with experimental validation.

RESULTS

Species-dependent variation in spindle motion of related nematode embryos during the first asymmetric cell division

We chose to explore which cellular parameters can explain the absence of spindle transverse oscillations in some nematode species,

while maintaining asymmetric positioning. Among those previously described by Valfort *et al.* (2018), we selected four species without spindle oscillations belonging to four distinct genera: *Pristionchus pacificus*, *Oscheius tipulae*, *Diploscapter species 1 JU359 (D. sp. 1)*, and *C. monodelphis*. We also chose *C. remanei and C. elegans* as control species displaying anaphase spindle oscillations. The differences in spindle dynamics are illustrated by one representative embryo per species (Figure 1, A–C). These species are also characterized by variations in cell size. For instance, *P. pacificus* embryos are 10% longer and *D. sp. 1* are 20% shorter than *C. elegans* embryos (Supplemental Table S1). As previously shown for a larger set of species, the lack of spindle oscillation is not restricted to small or large embryos; thus cell size change alone is unlikely to be responsible for evolutionary changes in spindle oscillations (Valfort *et al.*, 2018). We also estimated cell cycle length by measuring the time spent between the first nuclear envelope breakdown and the onset of the first cytokinesis, from the time-lapse recordings. We found that the cell cycle was shortest in *C. elegans* and *C. remanei*. *O. tipulae* and *P. pacificus* are 1.7× slower than *C. elegans*, whereas *C. monodelphis* and *Diploscapter sp.* 1 are 2.2× and 3× slower than *C. elegans*, respectively (Supplemental Table S1), raising the possibility that spindle oscillations are restricted to rapidly dividing species. However, because oscillations arise due to MT—motor interactions, we first proceeded to examine whether the kinetics of pulling can explain the differences in oscillation onset in some species but not others.

Dynamics of anaphase spindle pulling varies independent of oscillations across species

Previous work has shown that spindle movement, including oscillations, is mainly driven by pulling forces acting on the spindle in *C. elegans* embryos (Labbé *et al.*, 2004; Grill *et al.*, 2001). However, in some distant species, for instance in the yeast *S. pombe* (Tolić-Nørrelykke *et al.*, 2004), and during meiotic divisions in some cell types, for instance some oocytes' meiotic divisions, spindle positioning is independent of microtubule-based pulling forces from the cortex (Almonacid *et al.*, 2014). We first asked whether the absence of spindle oscillations in some nematode species reflects a mechanism that is independent of pulling forces. Mechanical forces acting on the spindle can be revealed by laser ablation of the central spindle at the onset of mitosis. Following spindle cutting, the centrosomes recoil toward the cell pole if they are initially pulled (Grill *et al.*, 2001). This is because the central spindle connects the poles and holds the balance, much like a stretched rubber band. In species in which the mitotic spindle elongates by inside-out pushing forces, severing the spindle leads to the collapse of the centrosomes at the center of the spindle (Khodjakov *et al.*, 2004; Tolić-Nørrelykke *et al.*, 2004).

We used a pulsed UV laser to sever the spindle at the onset of anaphase in all six species (Figure 2A; Supplemental Figure S1) and analyzed the recoil trajectories of the anterior and posterior centrosomes after the cut. The centrosomes of most of the species appear to recoil toward the cell pole (Figure 2B). The movement of *D. sp. 1* centrosomes was very limited (Figure 2B), with the characteristic recoil time being almost as long as the time of acquisition (27 s), with $\tau = 35.75$ and 25 s for the anterior and posterior pole, respectively. We found a velocity of ~0.02 and 0.11 μm/s for the anterior and posterior pole, respectively. This is suggestive of a near absence of recoil in *D. sp. 1*. Spindle poles of *C. elegans* and *C. remanei*, on the other hand, recoil faster, with half times of ~9 and ~5 s for anterior and posterior poles, respectively. Compared with *C. elegans*, the A/P average recoil time of *C. monodelphis* is longer, but *P. pacificus* and *O. tipulae* are statistically comparable (Figure 2C). The recoil velocity of *C. elegans* centrosomes after cutting is ~1.17 μm/s (anterior) and ~1.82 μm/s (posterior), a difference of ~36% (Figure 2D; Supplemental Table S2). This asymmetry in anterior and posterior pole recoil velocity is comparable to that in previous reports (Grill *et al.*, 2001), and the ratio is identical in *C. remanei* centrosomes. Interestingly, we found a lack of significant A/P asymmetry in recoil half-times and velocities for *C. monodelphis, P. pacificus*, and *O. tipulae*, despite their asymmetric cell division (see below for more discussion on this result).

Thus, we find that recoil trajectories of centrosomes after laser ablation cut vary between species in terms of the recoil velocity, half-time of recoil, final position of the centrosome, and anterior and posterior asymmetry (Figure 2, B and C). For all species that do not display oscillations, the half-time of recoil was longer than that of *C. elegans*, whereas the initial velocity was systematically lower. While these results suggest that forces acting on the spindles could explain the differences between anterior and posterior centrosomes for some species, we need to estimate the forces. To do this from the recoil experiment requires measuring the effective cytoplasmic viscosity that opposes the motion.

Cytoplasmic viscosity changes sixfold between closely related species

Visual inspection of the image time-series suggested qualitative correlation between spindle mobility patterns and passive mobility of these granules. Additionally, from first principles of fluid mechanics, the mobility of intracellular organelles and structures is expected to experience viscous drag and be an important determinant in their motion. The spindle mobility differences could thus most simply be explained by evolutionary changes in cytoplasmic viscosity and provide a direct link to spindle motion. To test this hypothesis, we proceeded to estimate the cytoplasmic viscosity across the species.

In DIC images, nematode embryo cytoplasm is prominently packed with clearly visible yolk granules (Clokey and Jacobson, 1986; Hermann *et al.*, 2005). We estimate cytoplasmic viscosity in the different species using granule mobility, as previously used for *C. elegans* embryo (Grill *et al.*, 2001). Because granules undergo streaming due to spindle movements and at times are even actively transported, we chose to follow granule mobility during interphase and in the top plane of the embryos, far from the spindle plane, to minimize the effects of active transport on the granule mobility measurement. We expect the mobility of the granules to be largely diffusive, that is, thermal random motion, and test this assumption (Figure 3A; see *Materials and Methods*). All further analysis of granule diffusive motility was performed only in the top plane, based on this difference in granule mobility. Embryo images were partitioned into anterior, middle, and posterior regions, and over 1000 granules in the anterior posterior portion of each embryo were tracked (Figure 3B) using a previously developed MATLAB code for single-particle tracking in DIC images (Chaphalkar *et al.*, 2021). Multiple embryos of each species were analyzed and the mean squared displacement (MSD) of granules was calculated (see *Materials and Methods*, Equation 4). Granule MSD plots were averaged over time and across multiple granules and fitted to the diffusion model (Figure 3C; *Materials and Methods*, Equation 5). Individual granules display apparent heterogeneity in MSD profiles, with some granules appearing to be superdiffusive, while others appear to follow subdiffusive profiles. On the average, they appear diffusive, due to the linear nature of the MSD plot at short time scales (Supplemental Figure S2 and *Materials and Methods*). We proceeded to fit Equation 4 (*Materials and Methods*) to the data in order to estimate a single free parameter, the effective

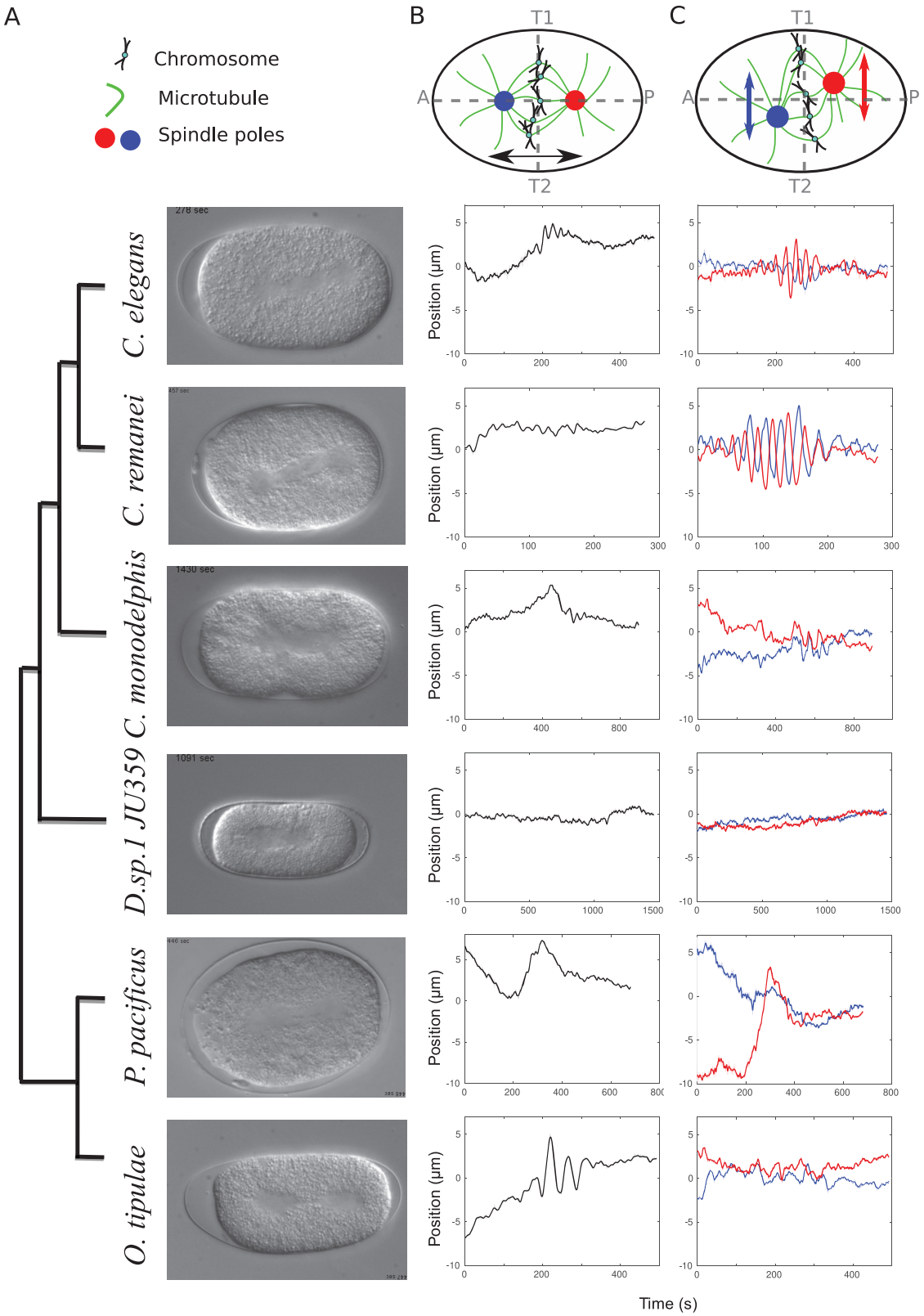

FIGURE 1: Diversity of spindle dynamics across nematodes. (A) The diversity in spindle movement in single-celled embryos of evolutionarily related nematodes is illustrated with one representative image per species taken from the study by Valfort *et al.* (2018). (Left) The phylogenetic relationship between the chosen nematode species and (Right) representative still images of single-celled embryos acquired in DIC are shown. Spindle and centrosome positions were tracked over time from DIC time series movies. (B) The change in position of the spindle midplane along the AP axis with time is plotted relative to the cell center (black lines). The position 0 µm is the intersection between AP and T1–T2

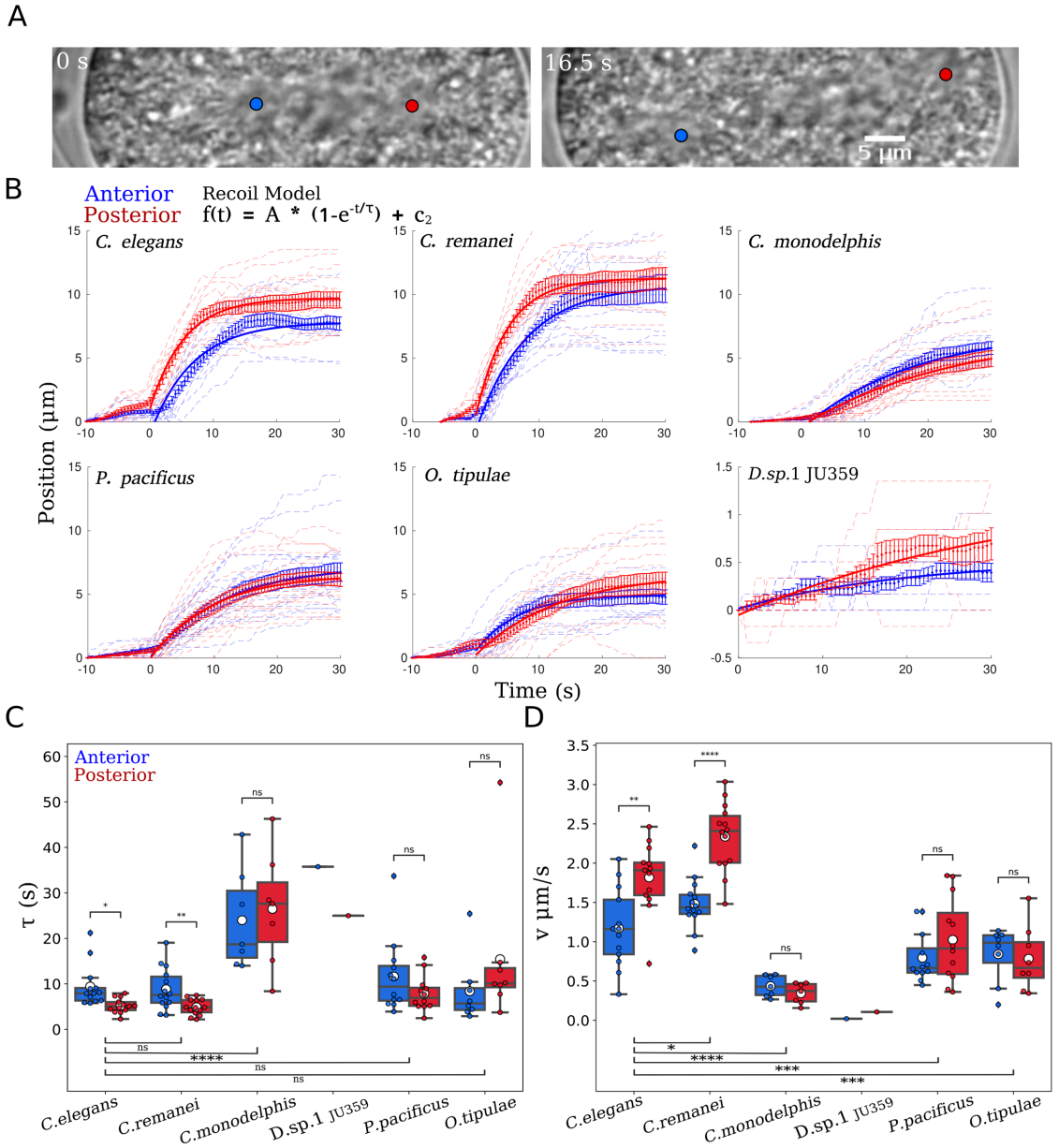

FIGURE 2: Centrosome trajectories post laser ablation characterized by recoil velocity and decay constant. (A) Representative images of a *C. elegans* embryo before (0 s) and 16.5 s after laser ablation of the spindle, with the anterior (blue circle) and posterior (red circle) centrosomes marked. (B) Recoil trajectories of the anterior (blue) and posterior (red) centrosomes after laser ablation ($t = 0$ s) for different species were averaged (filled circles) with error bars indicating SEM. The data were fitted to the recoil model (bold line) given by Equation 8 (*Materials and Methods*). The individual profiles are also plotted (thin lines). (C, D) The fit parameter distributions for each species from the anterior (blue) and posterior (red) trajectories are plotted as box plots (τ: left, v: right) with mean (white circle), median (horizontal line), and first and second quartile (box) indicated. The differences between anterior and posterior parameters within a species were compared using a paired *t* test, while interspecies comparisons between means for each species were made using an independent *t* test. The asterisks indicate * $p < 0.05$, ** $p < 0.01$, *** $p < 0.001$, and **** $p < 0.0001$ while ns = not significant.

axes (dashed lines). Positive values correspond to posterior displacement, and negative values are toward anterior. (C) The positions of the anterior (blue) and posterior (red) spindle poles with time are plotted along the transverse axis (T1–T2). Cell equator: 0 µm (AP axis intersects T1–T2). (B, C) Time $t = 0$ s corresponds to the onset of nuclear envelope breakdown, visible in DIC recordings. The key to the schematic depicts the chromosomes (black), the microtubules (green), and the spindle poles (red and blue).

diffusion coefficient D_{eff}. To estimate the fluid phase viscosity (η_F), which implicitly combines cytoplasmic viscosity and the effect of cytoskeletal elements and organelles, we measured the radius of lipid granules from each species averaged across multiple individuals (Supplemental Figure S3). Using the Stokes–Einstein relation, as described in *Materials and Methods* and Equation 6 (Einstein, 1905; Berg, 1993), we arrive at a value of viscosity. Due to the visually apparent crowding of granules in the cytoplasm (Figure 3B; Supplemental Figure S2), we include the effect of crowding by the highly packed yolk granules by correcting for their density (*Materials and Methods*, Equation 7, Figure 3E), based on a standard theory of the effect of soft-sphere packing in a crowded colloidal suspension on viscosity (Quemada, 1977). An additional motivation for applying this correction is that the granules have a high packing fraction (ϕ_{2D}) and a diameter of ~0.3 μm, comparable to the size of the centrosomes (diameter ~2–4 μm). Indeed, granules occupy between 29 and 42% of the cell area (Table 1), varying between species (Figure 3E). The packing fraction is then used to estimate the effective cytoplasmic viscosity η_{eff}, (Figure 3F). We find it to be 6- to 10-fold higher than the fluid phase viscosity η_F (Table 1), accounting for both fluid-phase and crowding effects. The mean *C. elegans* effective cytoplasmic viscosity η_{eff} of 0.67 Pa s (Table 1, combining anterior and posterior) is comparable to previously reported values, which ranged from 0.1 Pa s (Garzon-Coral *et al.*, 2016) to 1 Pa s (Daniels *et al.*, 2006).

This estimate of viscosity is based on the hypothesis that diffusion is the primary process driving granule motion, that is, passive, thermal Brownian motion. As a further test of the influence of active transport on diffusion, we examined the effect of ATP depletion on granule mobility, which is expected to block active intracellular transport. If D_{eff} is truly representative of the passive Brownian motion of granules, ATP depletion should not change the diffusion coefficient. Therefore, *C. elegans* embryos were treated with RNAi against *atp-2* (ATP synthase subunit) or *cyc-1* (Cytochrome-c1) as seen in Supplemental Figure S4A, which was shown to inhibit mitochondrial ATP production (Tsang *et al.*, 2001; Dillin *et al.*, 2002; Neves *et al.*, 2015). While it is expected that depleting ATP will affect all physiological processes in a nonspecific manner, the yolk granule mobility of treated compared with untreated *C. elegans* embryos was found to be quantitatively unchanged in terms of MSD profiles (Supplemental Figure S4B), the diffusion coefficient (Supplemental Figure S4C) and viscosity (Supplemental Figure S4D). Taken together, the evidence strongly supports the hypothesis that granule mobility we describe is indeed diffusive.

We find that effective cytoplasmic viscosity (η_{eff}) differs between species. Compared to *C. elegans*, the five other species show viscosity values that are significantly different. *C. monodelphis* shows the highest viscosity of 2.8 Pa s (Figure 3E; Table 1). We also find that viscosity differs greatly between anterior and posterior regions in *O. tipulae*, and to a lesser extent in *C. monodelphis* and *P. pacificus*, and only minimally (factor of 1.1) in *C. elegans*. The viscosity in the anterior and posterior halves of the embryos was, however, similar in *C. remanei* and *D. species 1* (Figure 3E; Table 1). These results reveal that even closely related species show a diversity in cytoplasmic viscosity, with an ~7-fold difference between the most extreme values measured.

While the increase in viscosity across species (Figure 3E) correlates qualitatively with slower recoil dynamics in spindle-cutting experiments (Figure 2, C and D), it is unclear if that can explain, for example, the absence of bona fide spindle oscillations in some species such as *P. pacificus*, whose cytoplasmic viscosity is very close to that of *C. elegans*. Therefore, we proceeded to examine whether the magnitude of the pulling forces on the spindle may also vary between species.

The net pulling forces and elasticity forces acting on centrosomes also vary between closely related nematode species

While spindle laser ablation experiments have been used in the past to estimate relative rates of pulling by forces acting on the astral MTs, the quantification of absolute forces requires a mechanical model of the spindles, motors and the cytoplasm. In recent work the absolute forces centering *C. elegans* metaphase spindles of one cell–stage embryos has been estimated by measuring relaxation after mechanical perturbation and fitting to a model with both elastic and viscous components, that is, a viscoelastic model (Garzon-Coral *et al.*, 2016). Indeed, multiple studies have concluded that the mechanical properties of the cytoplasm are best explained by viscoelasticity (Berret, 2016; Fabry *et al.*, 2001). The Kelvin–Voigt (KV) model is invoked to account not just for the spring force (F) that acts on laser ablated centrosomes pulling them backward, but also for the viscous drag (γ) due to the presence of cytoplasm, crowding by granules, and the elasticity (k) of the half-spindle and actin meshwork (Figure 4A). The fact that most of the six species tested show a recoil of centrosomes on ablation suggests we can use the same physical model to understand the mechanics across species. Based on the KV model, the position of the centrosome as a function of time, $p(t)$, is fitted to the equation

$$p(t) = \frac{F}{k}\left(1 - e^{\frac{-kt}{g}}\right) + c_1 \qquad (1)$$

where F is the effective force driving the movement of the centrosome as it recoils after cutting, k is the elasticity of the medium, g is the drag coefficient, and c_1 is the position at time 0. Assuming that the centrosome and MT aster can be treated as a spherical object, the Stokes drag coefficient can be estimated from the expression

$$g = 6\pi\eta R \qquad (2)$$

Here, η is the viscosity of the medium and R represents the centrosome aster radius. While the centrosome is larger in size than the granules by a factor of 10, the fraction of area occupied is between 30 and 40% (Figure 3E). At such densities, crowding effects need to be considered, even if the crowdant is smaller than the diffusing particle (Muramatsu and Minton, 1988). The fluid phase viscosity (η_f) represents the combined effect of cytoplasmic viscosity, cytoskeletal networks, and organelles, which we estimate from the effective diffusion coefficient D_{eff} (Figure 3C; Table 1). The effective viscosity η_{eff} that combines the effects of granule crowding is then used further to estimate the viscous drag acting on the centrosome. While there is some uncertainty in estimating centrosome sizes (Supplemental Table S1), we simplify the drag estimates since the variability between individuals of a species is expected to be constant.

In the KV model, the centrosome position is governed by a pulling force F, here exerted on astral microtubules by cortical force generators proportional to the deformation from resting length and the elasticity k that results from a combined effect of cytoplasmic components, actin meshwork, and astral MTs and the viscous drag g, which measures the opposition to the motion of the aster. Given the free parameters, a good fit to the recoil trajectories requires constraints. We use the effective cytoplasmic viscosity η_{eff}, as discussed above, to constrain the drag coefficient g (Equation 2; *Materials and Methods*). Centrosome sizes are

Species	Fluid phase viscosity of cytoplasm, η_F (Pa s)		Granule radius (μm)	Packing fraction, ϕ_{2D}		Effective cytoplasmic viscosity corrected for packing fraction, η_{eff} (Pa s)	
	Anterior	Posterior		Anterior	Posterior	Anterior	Posterior
C. elegans (*n* = 19)	0.14 ± 0.04	0.16 ± 0.04	0.32	0.33	0.35	0.63 ± 0.17	0.71 ± 0.18
C. remanei (*n* = 8)	0.13 ± 0.01	0.11 ± 0.03	0.34	0.29	0.33	0.47 ± 0.05	0.41 ± 0.11
C. monodelphis (*n* = 15)	0.22 ± 0.12	0.35 ± 0.17	0.32	0.42	0.41	1.78 ± 0.97	2.80 ± 1.40
D. sp. 1. JU359 (*n* = 5)	0.27 ± 0.10	0.27 ± 0.10	0.33	0.4	0.42	2.08 ± 0.75	2.07 ± 0.76
P. pacificus (*n* = 13)	0.12 ± 0.04	0.09 ± 0.03	0.31	0.4	0.4	0.70 ± 0.24	0.56 ± 0.18
O. tipulae (*n* = 14)	0.11 ± 0.04	0.15 ± 0.06	0.36	0.4	0.4	0.59 ± 0.20	0.85 ± 0.35

The viscosity of nematode embryonic cytoplasm from six species was estimated based on tracking the diffusion of ~1000 lipid granules (per species) to calculate MSD profiles (Figure 3, A–C, and Supplemental Figure S2). The fluid phase viscosity (η_F) for all six species was calculated from the effective diffusion coefficient obtained by fitting the MSD (Equation 5 in *Materials and Methods*) to the MSD profiles (Supplemental Figure S2). To account for self-crowding by a high density of lipid granules, we measured their radii (μm) and area packing fraction (Φ_{2D}) in order to correct the viscosity based on Equation 7 (*Materials and Methods*) to arrive at the effective viscosity η_{eff} (Pa s). Between 8 and 19 embryos were analyzed per species, indicated by *n*. All values of viscosity are mean ± SD.

TABLE 1: Measurement of cytoplasmic viscosity.

estimated based on their smooth disk-like appearance, which excludes the cytoplasmic granules due to the high density of astral microtubules around the pericentriolar material, as seen in DIC microscopy images. The radius of this disk serves as a measure for centrosome size for each species (Supplemental Table S1). This simplification is necessary because a centrosome is a complex structure with many microtubules extending from it, preventing precise measurement of a radius. Also implicit in our approach is the assumption that centrosome size remains constant during anaphase. Substituting these values into Equation 2 (*Materials and Methods*), we reduced the free parameters of the fit to only two, the force *F* and rigidity *k*, which were estimated from fits to the data from multiple recoil experiments.

Our results revealed the net pulling forces acting on the anterior and posterior centrosome of *C. elegans* spindles to be 42.2 and 101.7 pN, respectively (Figure 4C; Table 2). The A/P asymmetry in pulling forces acting on half spindles is found only in *C. elegans* and *C. remanei*, with A/P force asymmetry absent in all the remaining species (Figure 4C). This result is in apparent contradiction with the fact that all species divide asymmetrically. However, in these species, as in *C. elegans*, the entire spindle is slightly shifted posteriorly at the onset of anaphase (Supplemental Figure S1, A and B). We hypothesize that this initial asymmetry is sufficient to maintain the spindle in an asymmetric position, despite symmetric pulling forces during late anaphase. We find that *C. elegans*, *C. monodelphis*, and *P. pacificus* spindles experience comparable magnitudes of forces. However, compared with those in *C. elegans*, those in *C. remanei* and *O. tipulae* are lower, while *D. sp.1* appears to have the lowest values measured among all six species. Differences in pulling forces are very limited (~threefold) for most species, except for *D. sp. 1*, which is 15 to 20 fold smaller than *C. elegans*.

The rigidity (*k*) values range between ~2.8 and ~11.4 pN/μm, consistent with values reported for *C. elegans* embryonic spindle elasticity associated with centering (Garzon-Coral *et al.*, 2016). Although variations of the rigidity appear more constrained than those of pulling forces, they show a similar trend between species. Here, only *C. remanei* and *C. elegans* show clear A/P differences in elasticity (Figure 4C; Table 2).

The differences in spindle mechanics between species in terms of pulling forces, elasticity, and viscous drag suggest a global trend that might explain differences in unperturbed spindle behavior. To investigate this, we proceed to correlate these variables in order to find patterns.

Toward the definition of a parameter space for spindle positioning and oscillations

Overall, our results show substantial and independent variation, even between closely related species (Figure 3E and 4C; Tables 1 and 2). Interestingly, we find that the spindle dynamics measured by recoil velocity *v* (Figure 5A) and time constant τ after cutting (Figure 5B) correlates strongly with effective cytoplasmic viscosity ($|r| > 0.7$). We find little correlation between viscosity and the spindle pulling forces (Figure 5C) and elasticity (Figure 5D). To our surprise, cell-cycle time shows a strong correlation with viscosity with $r > 0.8$, although more species need to be examined to confirm this trend (Figure 5E; see *Discussion*). Cell length, which we would have expected to affect the recoil properties only weakly, correlates with the recoil velocity *v* and time of recoil τ (unpublished data).

In the crowded environment of the cell, it is not surprising that viscosity plays an important role in intracellular mobility. When we measure the average unperturbed spindle oscillation speed of intact spindles (see *Materials and Method* and Supplemental Figure S5) and correlate it with viscosity, we find that species with low viscosity have faster-oscillating spindles, while more viscous cytoplasms result in slower oscillations. The plot of oscillation speed with viscosity is not sufficient to distinguish species that show bona fide oscillations (Ce, Cr) from the rest (Pp, Ot, Dsp, and Cm) that do not (Figure 5F). This contradicts the prediction from a previously developed model that increasing the viscosity of *C. elegans* cytoplasm would lead to a smooth reduction in spindle oscillation speed (Kozlowski *et al.*, 2007), which we can fit to a 4-parameter sigmoid function (Equation 9; *Materials and Methods*). The fit resulted in a minimal oscillation speed of 0.15 μm/s (*y*-axis of Figure 5F) that we use as a quantitative measure for the loss of oscillations, to separate the experimental data of spindle oscillation speeds into "oscillating" and "nonoscillating." By comparing the predictions from previous work (Kozlowski *et al.*, 2007) with comparative measurements using evolutionary diversification of properties, we overcome the difficulty of experimentally testing the effect of changing viscosity, since it is expected to have nonspecific effects on cell physiology.

However, viscosity alone appears to be insufficient as a predictor and sole determinant of loss of oscillations, as seen in the similar values of viscosity in *C. elegans*, *P. pacificus*, and *O. tipulae*, where only one shows bona fide spindle oscillations. Other parameters such as spindle–pulling forces, which are the primary determinant of spindle oscillations, and characteristic cell size, which sets the spatial scale, could be important. We expect that a tradeoff between

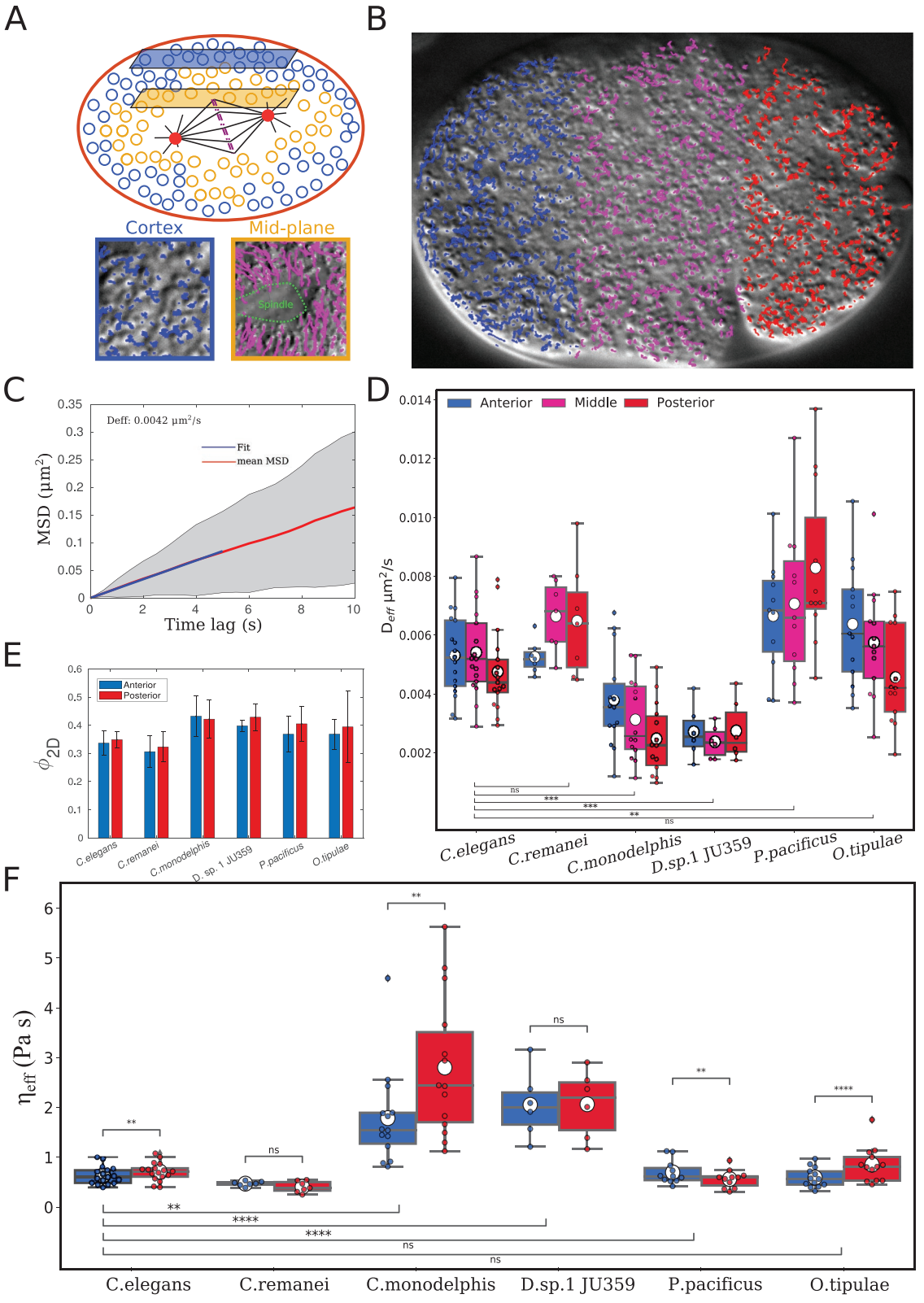

FIGURE 3: Cytoplasmic viscosity estimates from yolk granule mobility. (A) Yolk granule mobility in the one-celled stage of the nematode embryo from midplane (yellow circles) and cortical (blue circles) is depicted. Lines: tracks of granules, midplane: yellow box, and cortex: blue box. (B) Granule movement was automatically tracked from DIC microscopy time series of a *C. elegans* embryo imaged in the cortical plane. Lines: tracks, blue: anterior, magenta: middle, and red: posterior. (C) The mean squared displacement (MSD) averaged over granules from the whole embryo is plotted as a function of time interval (red line). Data are fitted to a diffusion model (blue line, Equation 4,

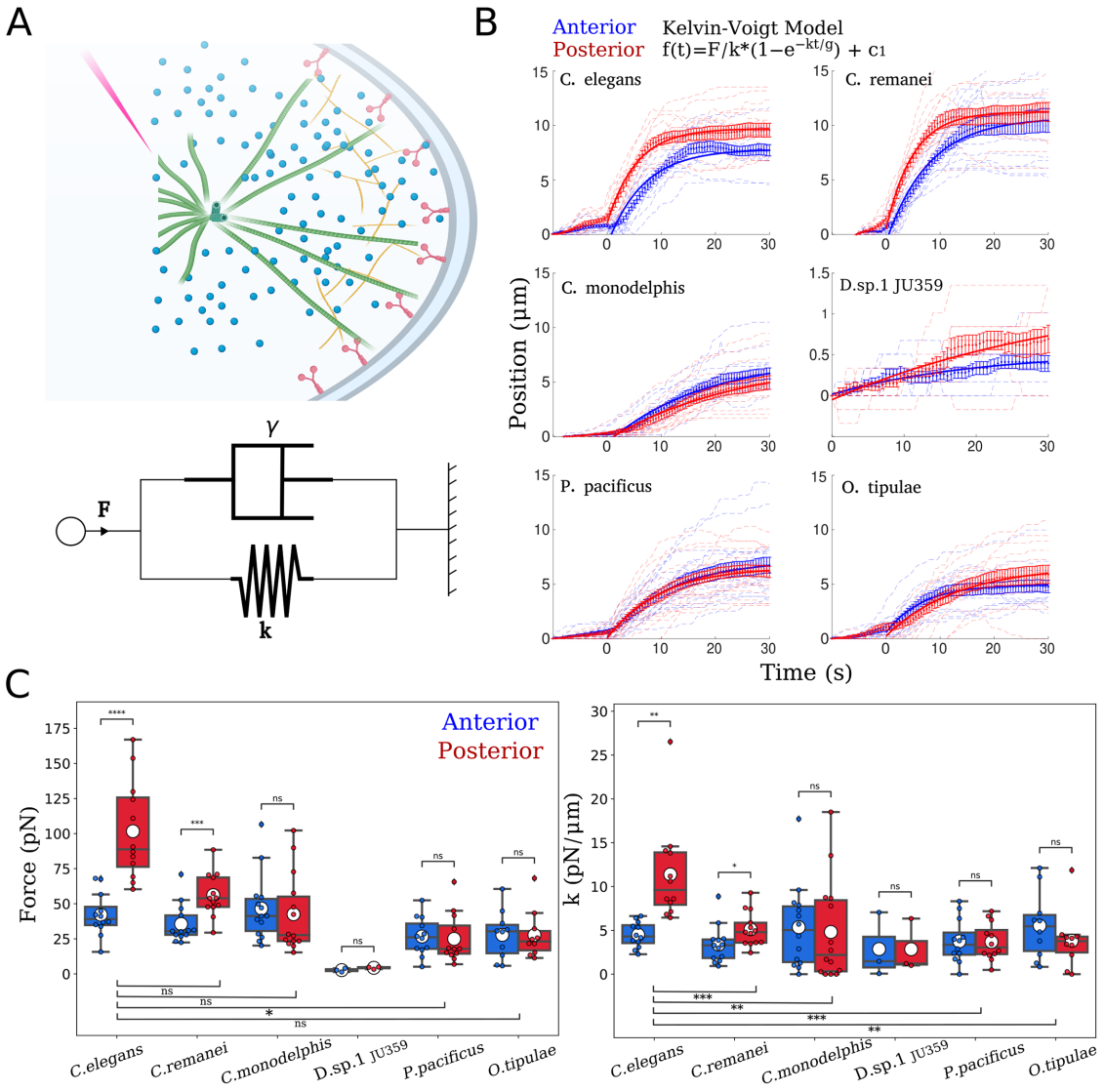

FIGURE 4: Pulling forces estimated from viscoelastic model fit to recoil data. (A) Schematic of laser ablation of the spindle midplane that results in recoil motion of the centrosome modeled by the Kelvin–Voigt viscoelastic model represented here by a spring with elasticity *k* and a dashpot with viscous drag coefficient γ, which acts to damp movement due to the pulling force *F*. (B) Recoil trajectories of the anterior (blue) and posterior (red) centrosomes after laser ablation for different species were averaged (filled circles). Error bars: SEM. The mean data were fitted to the Kelvin–Voigt model (bold line), Equation 1 (*Materials and Methods*). The faint dashed lines represent individual profiles of anterior (blue) and posterior (red) centrosomes. (C) The distributions of the fit values of force, *F* (Left), and elasticity, *k* (Right), for each species from the anterior (blue) and posterior (red) trajectories are plotted as box plots with mean (white circle), median (horizontal line), and first and second quartile (box) indicated. The differences between anterior and posterior within species were compared using a paired *t* test, while interspecies comparisons were done using an independent *t* test, similar to Figure 2. The asterisks indicate * $p < 0.05$, ** $p < 0.01$, *** $p < 0.001$, and **** $p < 0.0001$, while ns = not significant.

Materials and Methods). Gray region: SD across individual trajectories ($n \sim 4{,}000$). Fit parameter $D_{eff} = 0.0042$ µm^2/s. (D) The D_{eff} of anterior, middle, and posterior cortical granules from all six species are represented as box plots. (E) The area packing fraction of granules (ϕ_{2D}) from the anterior (blue) and posterior regions (red) is plotted for the six nematode species analyzed (mean ± SD). (F) The effective viscosity η_{eff} of each nematode species from the anterior (blue) and posterior (red) regions is plotted as a box plot. White circle: mean, horizontal line: median. Points indicate outliers. The asterisks indicate * $p < 0.05$, ** $p < 0.01$, *** $p < 0.001$, and **** $p < 0.0001$, while ns = not significant for *t* tests (paired within species, independent between species).

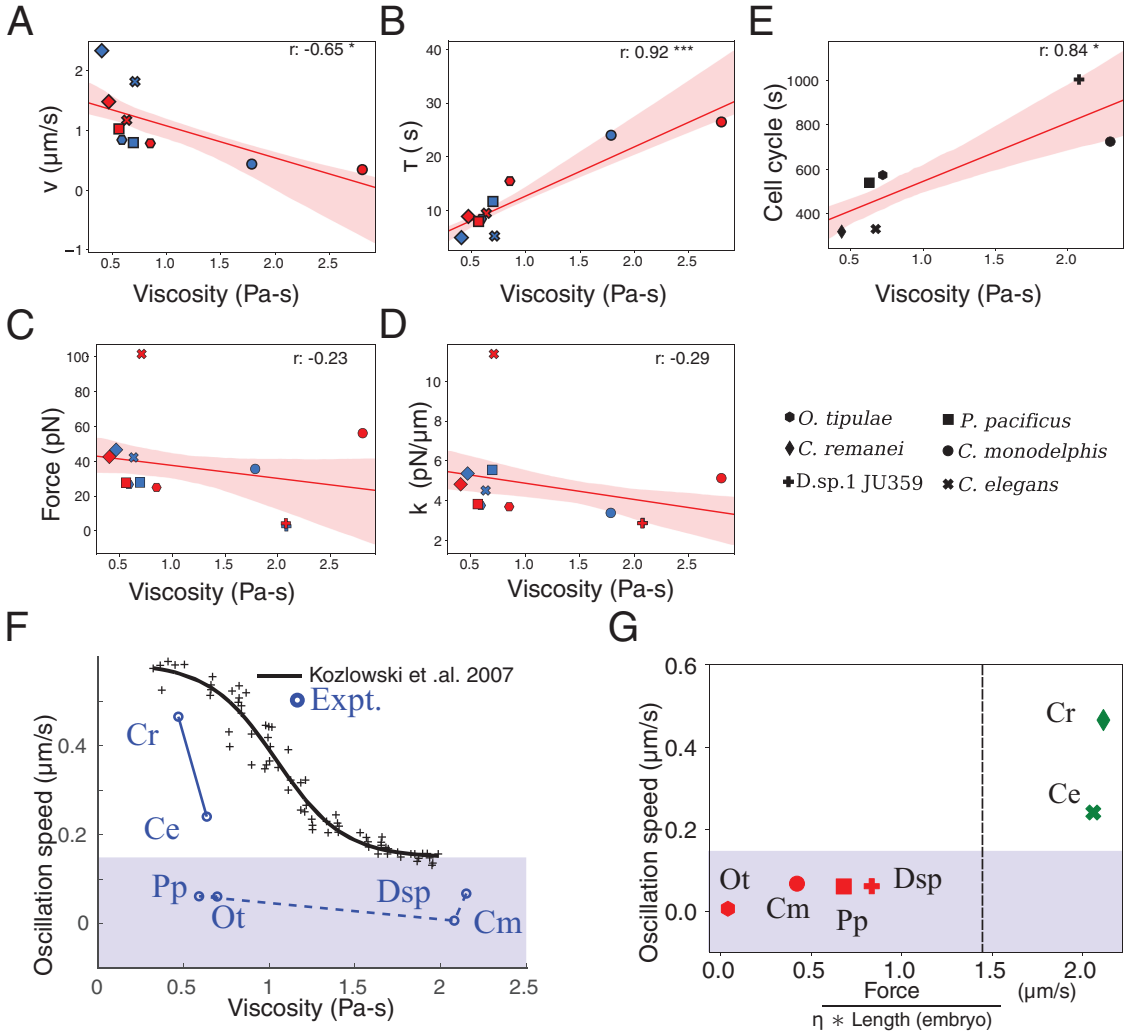

FIGURE 5: Effect on spindle mobility of divergence in cell mechanics. The covariation in all six species of (A) recoil velocity *v*, (B) decay constant τ, (C) spindle-pulling force (pN), (D) elasticity (pN/µm), and (E) cell cycle time with effective viscosity are plotted. Symbols: species, red line: regression fit, shaded area: one SD (confidence interval 0.68), *r*: Pearson's correlation coefficient, * $p < 0.05$, ** $p < 0.01$, *** $p < 0.001$, **** $p < 0.0001$ (significance levels). (F, G) Spindle oscillation speeds (from Supplemental Figure S6) are plotted as a function of the effective viscosity, and ω, G. F, experimentally measured spindle oscillation speed: circles (o), simulations (Kozlowski *et al.*, 2007): plus sign (+). Simulation data were fitted to a four-parameter sigmoid function (Equation 9, *Materials and Methods*). Fit parameters: maximal speed $a = 0.44$ µm/s, minimal speed $d = 0.15$ µm/s, viscosity at half-maximal oscillation speed $c = 1.04$ Pa-s, and steepness parameter $s = 0.2$ Pa.s. G, the oscillation speed of the spindle is plotted as a function of ω, the ratio of the pulling force to the product of viscosity and the length of the embryo ($\omega = F/(\eta \times L)$). The dashed line is the midpoint separating oscillating from nonoscillating species. F, G, shaded regions (purple): oscillation speeds less than the minimal speed $d = 0.15$ µm/s from the fit to simulation data in F. Ce: *C. elegans*, Cr: *C. remanei*, Ot: *O. tipulae*, Pp: *P. pacificus*, Dsp: *Diploscapter sp. 1*, and Cm: *C. monodelphis*. Colors indicate nonoscillating (red) and oscillating (green) species.

viscosity and pulling forces could explain sustained oscillations. This is supported by the case of *C. remanei*, in which spindles oscillate similarly to those in *C. elegans*, whereas both force and viscosity are lower in comparison (Figure 3E, 4C). On the other hand, *P. pacificus* experiences smaller forces than *C. elegans* but only small differences in viscosity, which could explain the absence of oscillations. To account for a potential tradeoff between the pulling forces and viscous drag that opposes it, and inspired by previous work by Juang *et al.* (2017) on the evolutionary scaling of mechanical stiffness of avian eggs by a dimensionless parameter combining mass, elasticity, and egg size, we estimate a ratio ω that combines spindle pulling forces (*F*), viscosity (η), and embryo size (*L*). We define it as

$$\omega = \frac{F}{\eta L} \tag{3}$$

where η is the effective viscosity and *L* is the long axis of the embryo. While this measure has dimensions length/time, we find that it may predict the propensity of spindles to oscillate. We find that spindle oscillation speed plotted as a function of ω (with units µm/s) shows a clear separation between the species and appears to predict the onset of oscillations, with the midpoint between Pp and Cr (ω = 1.44) serving as this threshold (Figure 5G). A low value of the ratio is suggestive of either low force or high viscosity, while a high value indicates either low viscosity or high force, both normalized by

Species	Force (pN)		K (pN/μm)	
	Anterior	Posterior	Anterior	Posterior
C. elegans (*n* = 14)	42.21 ± 15.43	101.67 ± 35.24	4.50 ± 1.45	11.38 ± 5.58
C. remanei (*n* = 14)	35.61 ± 13.90	56.15 ± 15.31	3.37 ± 2.15	5.12 ± 1.97
C. monodelphis (*n* = 14)	46.62 ± 23.62	42.55 ± 27.96	5.36 ± 4.77	4.81 ± 5.81
D. sp. 1. JU359 (*n* = 2)	2.70 ± 1.32	4.35 ± 0.88	2.87 ± 3.70	2.85 ± 3.03
P. pacificus (*n* = 16)	26.68 ± 13.60	24.97 ± 17.54	3.75 ± 2.52	3.68 ± 2.13
O. tipulae (*n* = 10)	27.82 ± 17.28	27.74 ± 17.05	5.54 ± 3.82	3.82 ± 3.26

Individual trajectories of centrosome recoil data from spindle cutting were fitted to the Kelvin–Voigt model and fit parameters averaged for each species. Centrosome sizes were measured from DIC images of spindles based on the maximal diameter of the clear region of the spindle poles. Brackets indicate the number of trajectories analyzed (*n*). Only those fits with $R^2 \geq 0.80$ (0.50 for *D. sp.1* JU359) were used for analysis.

TABLE 2: Fit parameters based on the Kelvin–Voigt model.

embryo size. Thus the measure ω appears to predict the onset of anaphase spindle oscillations in the species examined.

DISCUSSION

The intracellular aqueous environment of macromolecules and presence of cytoskeletal proteins has made the study of viscous and elastic properties of cells vital for our understanding of cellular mechanobiology. However, how much these properties can change without affecting the functions they sustain is unclear. This is in part because experimental perturbations of these properties are challenging. An alternative approach is to measure the physical properties of cells from different species, because they reveal the range of solutions retained over the course of evolution, and hence the range of possible changes.

In this study, we aim to explore the reason that spindle motion varies between closely related species of nematodes. We had previously identified species for which spindle elongation and displacement at anaphase is accompanied by transverse oscillatory movements, similarly to the situation found in *C. elegans*. In contrast, many nematode species do not undergo these oscillations, despite an identical off-center displacement of the spindle at anaphase. Comparing spindle movements is a difficult task because spindle elongation, displacement, and oscillations occur simultaneously. Moreover, the spindle is composed of two centrosomes that are oscillating in an anti-phase manner and that are linked by a central spindle, whose mechanical properties are mainly unknown. Based on previous work demonstrating the role of motor-driven pulling forces (elastic) and the effect of cytoplasmic drag in damping this movement (viscous), we proceeded to examine the comparative viscoelastic properties of the spindle motion of multiple species. As a first step, we laser-ablated the central spindle and analyzed the recoil trajectories to estimate velocity and characteristic time constants. However, a viscoelastic model required an estimate of viscosity between species. Using the diffusive motion of high-contrast cytoplasmic granules, we found a 10-fold variation in the viscous drag. Using the drag to constrain a viscoelastic model of spindle recoil, we find that spindle elasticity and pulling forces vary by a factor of ~4, except for *D. sp. 1* (forces are ~20× smaller than in *C. elegans*). Correlation of intact spindles, as well as recoil dynamics, suggests that a balance of forces acting on spindles determines the mobility. Cellular parameters such as centrosome size or cell length do not appear to correlate with spindle recoil parameters, while viscosity correlates strongly with recoil parameters τ and *v*. However, it does not separate species whose spindles exhibit bona fide oscillations from those whose spindles do not. Inspired by studies to quantify egg stiffness by a single dimensionless number that revealed allometric invariance of avian egg mechanics (Juang *et al.*, 2017), we arrived at a measure of spindle stiffness ω, the ratio of force and viscosity scaled by embryo size. This ratio can successfully predict a threshold for the emergence of spindle oscillations above a critical value that could serve as a biophysical constraint on the evolution of spindle oscillations. Quantitative intracellular measurements of viscosity and spindle forces in multiple species will be required to test the validity of this prediction.

An important aspect of our study is the absolute quantification of drag, elasticity, and forces acting on spindles. While measurement errors are inherent in any method, the error in size estimation of centrosomes is comparable across species, suggesting that while more precise estimation of sizes will improve the accuracy of our estimates of spindle mechanics, it will not affect the relative trends. Indeed, by considering a predictive ratio between the pulling force and opposing viscosity, we possibly have a robust measure less sensitive to errors in measurement.

Our results first demonstrate that regardless of the presence of spindle transverse oscillations, all studied species are subjected to cortical pulling forces. Interestingly, although dynein is a highly conserved protein, the proteins responsible for its anchoring at the cortex, GPR-½ or LIN-5, are not found in the genomes of *P. pacificus*, *O. tipulae*, or other members of the *Diploscapter* genus (Delattre and Goehring, 2021). This raises the possibility that although the pulling machinery is conserved, the molecular complex responsible for this force has diverged rapidly between closely related species. We found variations in the net pulling forces by a factor of ~3 for most species except *D. sp. 1*. Previous models have proposed that modulation of the force can be achieved by changes in the number of motors, the individual force per motor, the attachment and detachment rate of motors, and microtubule dynamics, as seen in other systems (Sutradhar *et al.*, 2015; Jain *et al.*, 2021). Establishing transgenic lines in these different species, in particular to follow live microtubules, is a necessary step toward more quantitative measurements of these parameters.

We also find that the rigidity (spring elasticity) parameter varies between the species measured by a factor of ~4, ranging between 2.9 and 11.4 pN/μm (Figure 4C and Table 2). In terms of the cellular components, this parameter can be understood to be a combined measure of cytoplasmic stiffness and microtubule components. The lack of a clear trend suggests that while the effective elasticity due to cytoplasmic inclusions and the density of microtubules and actin meshwork vary between closely related nematode species, they appear to correlate only weakly with spindle mobility. To dissect the molecular components that govern this effective elasticity parameter in future, a fluorescence-based approach to comparing these

meshworks could help understand why this mechanical parameter does not appear to play a role in spindle dynamics. This suggests that the forces of spindle pulling and drag are the primary determinants of spindle behavior in these species.

Embryonic division in all the species examined here is asymmetric. Yet our study finds that only *C. elegans* and *C. remanei* have measurably distinct A/P asymmetry in spindle pole retraction half-times and velocity (Figure 2B), as well as pulling forces estimated (Figure 4C). The asymmetry of the spindle pole displacement can arise due to differences in forces driving translocation, in the initial position, or in both. We found that all species have a posteriorly shifted spindle at the onset of anaphase, similarly to what had been described for *C. elegans* (Supplemental Figure S1; Labbé *et al.*, 2004; Grill *et al.*, 2001). In *C. elegans*, the initial shift of the spindle at metaphase and early anaphase is due to the asymmetry of pulling forces (Labbé *et al.*, 2004). Our results thus suggest that an early asymmetry in the pulling forces is sufficient to maintain an asymmetric position and ultimately an asymmetric cell division in most species, regardless of the asymmetry of pulling forces during the remainder of anaphase. Nevertheless, whether an imbalance of pulling forces is responsible for the initial shift in spindle positioning outside *C. elegans* remains to be demonstrated.

The evolutionary scaling of size, dynamics, and elongation has been reported for inbred lines of *C. elegans* and was explained by a model of 1–1 stoichiometry of astral MTs and cortical force generator (FG) complexes (Farhadifar *et al.*, 2020). Asymmetric spindle pulling in the model arises from a 20% greater number of FGs localized in the posterior of the cell. While this model addresses many of the limitations of previous physical models in explaining evolutionary diversification, the experimental data for reconciliation involve the use of inbred lines of the model. Therefore, by examining the nature of spindle dynamics and elongation in more than just *C. elegans*, we believe we see wider variation in measured properties, and identify potential constraints on the variability and the consequences of it in terms of cell size, viscosity, and forces.

Early work measuring cytoplasmic viscosity in vertebrate cell lines reported a viscosity of 0.282 Pa.s following the Brownian motion of cytoplasmic inclusions (Alexander and Rieder, 1991). A more recent study using micrometer-sized beads and magnetic tweezers to measure the viscoelastic properties of the cytoplasm in *C. elegans* during spindle positioning also reported viscosity of 0.159 Pa.s (Garzon-Coral *et al.*, 2016). However, tracking the microrheology of the mobility of injected nanospheres in one-celled embryos of *C. elegans* revealed a spatially uniform cytoplasmic viscosity of 1 Pa.s (Daniels *et al.*, 2006). Accumulating evidence of the probe size dependence of such measurements due to macromolecular crowding (Etoc *et al.*, 2018; Mogilner and Manhart, 2018) could explain this order-of-magnitude difference reported by different workers in the same species. Our measurements retrieve a viscosity value that is in between these two extremes for *C. elegans*. We report the effective cytoplasmic viscosity to be ~600 times higher than the viscosity of water. Using the same approach to multiple species, we have uncovered large variations, up to an order of magnitude, between species, with *C. monodelphis* showing the highest viscosity. The differences we measure could arise from multiple factors such as differences in protein concentrations, presence of different densities of cytoskeletal meshwork, or higher organelle densities. In future, a careful morphological comparison between the species could allow us to address the question of how these differences in viscosity could arise.

We also note that species that have high viscosity also have a longer cell cycle duration (Figure 5C; correlation coefficient R = 0.84). This result suggests that the only combinations that have been retained by natural selection are compensatory changes, where high viscosity is compensated for by a slowdown of the cell cycle or vice versa. Over the course of evolution, slow species could have afforded an increase in cytoplasmic viscosity because even though objects are slowed down by the viscous drag, they will have time to reach their final positions. Conversely, a low viscous drag may have preconditioned the emergence of a fast cell cycle. Regardless of the orientation of changes, this interesting correlation raises the question of the selective pressure responsible for species-specific viscosity values.

Overall, we find significant variations in all parameters and species-specific combinations of parameters, which are all compatible with asymmetric spindle positioning. How far these parameters can change without perturbing the first embryonic division remains an open question, but our study is a first step toward the exploration of this parameter space. The specific case of *D. sp. 1*, for which all parameters have changed dramatically from those for *C. elegans*, demonstrates how much change can be tolerated.

Back to our initial question, our results allow us to define which combinations of parameters are now compatible with spindle transverse oscillations. Reduction of pulling forces can still lead to oscillations provided it is compensated for by reduced cytoplasmic viscosity, as seen in *C. remanei*, per unit length of the embryo. However, changes in a single parameter, as seen in *P. pacificus* (reduced pulling forces) or in *C. monodelphis* (higher viscosity), critical for oscillations, do not suffice. We propose that a tradeoff between cortical pulling forces and cytoplasmic viscosity results in spindle oscillations when the ratio of pulling forces to viscosity is high for a given embryo size. This provides a framework that could be tested with more species of nematodes, as well as generalized to other cellular systems.

MATERIALS AND METHODS

Request a protocol through *Bio-protocol*.

Image acquisition of nematode embryos and strain maintenance

All strains were maintained at 20°C on nematode growth medium seeded with *E. coli* OP50, as described in (Valfort *et al.*, 2018): *Caenorhabditis elegans* (N2), *Caenorhabditis remanei* (PB219), *Caenorhabditis monodelphis* (SB341), *Diploscapter sp. 1* (JU359), *Oscheius tipulae* (CEW1), *Pristionchus pacificus* (PS312) (Valfort *et al.*, 2018). For embryo recording, females were dissected in M9 and one cell–stage embryos were placed between slide and coverslip on a 2% agar pad. Embryos were observed with a Zeiss Axioimager A1 or A2 with a 100× DIC Plan Apochromat NA 1.4 lens. For video recording of the cell division, we took two images per second with a digital Kappa camera (DX4-285FW).

RNAi experiments

RNAi experiments on *C. elegans* were performed by feeding. Wild-type L4 larvae were fed for 24 h, with HT115 bacteria producing the double-strand RNA of *atp-2* and *cyc-1* genes. We considered that RNA interference was achieved when the one-cell embryos did not show signs of spindle movements during mitosis.

Laser ablation

One-cell embryos in prophase or prometaphase were mounted between slide and coverslip as described above. Embryos were then recorded on an inverted spinning-disk confocal microscope (Leica DMI4000B- CSU 22 Yokogawa) with a 100× immersion objective

(HCX PL APO 1.4 oil) controlled by Metamorph. Images were acquired with an iXon3 897 Andor camera every 0.5 s. Spindle severing was performed using a UV laser module (λ = 355 nm) iLas2 Roper, as described in (Grill *et al.*, 2001). For each species, the laser power was adjusted so that the cut, performed at the onset of spindle elongation, generated a rapid movement of the centrosomes (due to spindle severing), but did not arrest the cells (due to excess laser power).

Granule-based viscosity measurement

DIC images of nematode zygotes were acquired every 0.5 s in the midplane of the embryo during prometaphase. Images were preprocessed to enhance contrast (with 0.3% saturated pixels) using Fiji (Schneider *et al.*, 2012). Granule motion was analyzed by tracking whole embryos and cropped regions of interest (ROIs) using a home-built program in MATLAB (Mathworks, USA) for single-particle segmentation and tracking of DIC images (Chaphalkar *et al.*, 2021). Granule data was averaged with ~1000 granules per embryo, with between 5 and 19 embryos per species analyzed. The MSD of particles was calculated using the *x*–*y* coordinates of tracked granules as follows:

$$MSD = < r^2 > = < \left[r(t+\delta t) - r(t) \right]^2 > \quad (4)$$

Here, r is the displacement of the particle at two time points separated by a time-step δt. We employ a sliding window approach and estimate the MSD for the first 3/4 of the data to avoid artefacts due to undersampling at large values of δt (Michalet, 2010; Khetan and Athale, 2016). Some of the MSD trajectories of individual granules appeared nonlinear (superdiffusive driven by an apparent drift, or subdiffusive due to restriction in movement), suggesting anomalous diffusion. To estimate the degree to which such deviations from simple diffusion occur in our data, we fitted an anomalous diffusion model ($4Dt^{\alpha}$) to the data and estimated the anomaly coefficient α (Athale *et al.*, 2014). The average value of $\alpha \sim 1$ confirms the diffusive nature of granule mobility. The range of values of the anomaly parameter have been described previously to be consistent with normal diffusion (Lanoiselée *et al.*, 2018). The effective diffusion coefficient (D_{eff}) was therefore estimated by fitting up to 5 s of the average MSD profile to the diffusion model,

$$MSD = < r^2 > = 4 \times D_{\text{eff}} \times t \quad (5)$$

where t is the time interval. The fluid viscosity (η_F) as estimated from the effective diffusion coefficient (D_{eff}) and the radius (r) of granules using the Stokes–Einstein relation,

$$\eta_f = K_b \times T / 6 \times \pi \times r \times D \quad (6)$$

Granule radii (r) are very similar ~0.2–0.3 μm across species (Figure S3) and are used to estimate the viscosity for each species. To account for the crowded nature of the cytoplasm due to granule packing, the effective viscosity (η_{eff}) was estimated based on the approximation for soft spheres (Quemada, 1977) by correcting for the packing fraction of the embryo due to the 2D granule-packing fraction (ϕ). The granule-packing fraction for each species was calculated from eight representative ROIs each from the anterior and posterior regions, with ~400 granules per species. The granule density per unit area, $\varrho_g = N_g / A_{\text{cell}}$, was estimated for the anterior and posterior 1/3 of each embryo along the major axis in each species (Figure 2D). The area of each granule (A_g) was measured from the granule radius to arrive at the granule packing fraction $\phi_{2D} = \varrho_g \times A_g$ and used to calculate the effective viscosity as

$$\eta_{\text{eff}} = \eta_f \times (1 - \phi_{2D} / \phi_{\max})^{-2} \quad (7)$$

where $\phi_{\max}$ is the maximal packing fraction, taken to be 0.64 for random packing (Buscall *et al.*, 1994), and η_f is the fluid phase viscosity. The packing fraction was measured from DIC images in the anterior and posterior regions of each species (Figure 2D).

Oscillation speed

Spindle oscillations were analyzed in representative trajectories of each species by measuring the distance of the centrosomes from the centerline, defined by the A–P axis, with time, and the data were smoothed using the discrete cosine transform to reduce low-frequency noise, with the threshold greater than 1.5 for *C. monodelphis* and *O. tipulae* and 0.56 for the remaining species (Supplemental Figure S5A). The speed of oscillation was calculated as the change of position over successive windows of 5-s intervals throughout the smoothed trajectory, and the distribution (Supplemental Figure S5B) was used to estimate mean oscillation speed for anterior and posterior centrosomes (Supplemental Figure S5C).

Data fitting

The initial recoil velocity and rate of decay from the recoil trajectories were obtained by fitting the anterior and posterior centrosome recoil trajectories to the function

$$f(t) = A \times (1 - e^{t/\tau}) + c_2 \quad (8)$$

where A is amplitude of recoil, τ is the decay constant of the exponential, and V is the recoil velocity given by $V = A/\tau$, based on previous work (Sumi *et al.*, 2018). Oscillation speed predictions from simulations as a function of increasing viscosity were taken from previous work by Kozlowski *et al.* (2007) by digitizing the plot (webplotDigitizer) and fitting it to a four-parameter sigmoid function described previously (Khetan and Athale, 2016),

$$v = d + \frac{a}{1 + e^{\frac{(\eta - c)}{s}}} \quad (9)$$

where v is the speed, η is the viscosity, d and a are the minimal and maximal speeds, c is the half-maximal viscosity, and s is the steepness of the profile. Individual data from centrosome recoil of all species were ignored if the goodness of fit measure (R^2) was less than 0.8, except for *D. sp. 1*, where this cutoff was 0.5. As a result of this, we do not report v and τ values for this species (Figure 5, A and B).

Statistical tests and correlations

All correlations were performed using the Pearson correlation test. *Regplot* was used to illustrate regression fits for all correlations (Seaborn 0.11.0, Python3). The size of the confidence interval was set to 68, which falls within 1 SD (Figure 5, A–E). All statistical tests were performed in SciPY 1.5.2. Correlations were quantified using the function for Pearson's correlation coefficient in Python, *pearsonr* (SciPy). Viscosity between species and within a species across A/P regions were compared using the *t* test.

ACKNOWLEDGMENTS

Anushree Chaphalkar and Tanmaya Sethi were involved in the early stages of the project. C.A. is grateful to Vijaykumar Chikaddi for discussions. M.D. thanks Fabien Montel for critical comments and discussions. M.D. and T.B. acknowledge the contribution of the imaging platform PLATIM from SFR Biosciences Lyon. Research in M.D.'s team was supported by a research grant from ANR-17-Tremplin-ERC2 001201. M.D. and C.A. are recipients of joint CEFIPRA

research grant 62T5-1. D.K. is supported by a fellowship from the Department of Biotechnology, Government of India (DBT/2018/IISER-P/1154). C.A. is supported for travel by a grant from the Indo-French Centre for the Promotion of Advanced Research, CEFIPRA (IFC/0036/2017/1222).

REFERENCES

Alexander SP, Rieder CL (1991). Chromosome motion during attachment to the vertebrate spindle: initial saltatory-like behavior of chromosomes and quantitative analysis of force production by nascent kinetochore fibers. J Cell Biol 113, 805–815.

Almonacid M, Terret ME, Verlhac MH (2014). Actin-based spindle positioning: new insights from female gametes. J Cell Sci 127, 477–483.

Athale CA, Dinarina A, Nedelec F, Karsenti E (2014). Collective behavior of minus-ended motors in mitotic microtubule asters gliding toward DNA. Phys Biol 11, 12.

Berg HC (1993). Random Walks in Biology. Princeton, NJ: Princeton University Press.

Berret JF (2016). Local viscoelasticity of living cells measured by rotational magnetic spectroscopy. Nat Commun 7, 10134.

Buscall R, D'Haene P, Mewis J (1994). Maximum density for flow of dispersions of near monodisperse spherical particles. Langmuir 10, 1439–1441.

Chaphalkar AR, Jawale YK, Khatri D, Athale CA (2021). Quantifying intracellular particle flows by DIC object tracking. Biophys J 120. doi:10.1016/j.bpj.2020.12.013.

Clokey GV, Jacobson LA (1986). The autofluorescent "lipofuscin granules" in the intestinal cells of *Caenorhabditis elegans* are secondary lysosomes. Mech Ageing Dev 35, 79–94.

Crowder ME, Strzelecka M, Wilbur JD, Good MC, von Dassow G, Heald R (2015). A comparative analysis of spindle morphometrics across metazoans. Curr Biol 25, 1542–1550.

Daniels BR, Masi BC, Wirtz D (2006). Probing single-cell micromechanics in vivo: the microrheology of *C. elegans* developing embryos. Biophys J 90, 4712–4719.

Delattre M, Goehring NW (2021). The first steps in the life of a worm: themes and variations in asymmetric division in *C. elegans* and other nematodes. Curr Top Dev Biol 144, 269–308.

Dillin A, Hsu AL, Arantes-Oliveira N, Lehrer-Graiwer J, Hsin H, Fraser AG, Kamath RS, Ahringer J, Kenyon C (2002). Rates of behavior and aging specified by mitochondrial function during development. Science 298, 2398–2401.

Einstein A (1905). Über die von der molekularkinetischen Theorie der Wärme geforderte Bewegung von in ruhenden Flüssigkeiten suspendierten Teilchen. Ann Phys 322, 549–560.

Etoc F, Balloul E, Vicario C, Normanno D, Liße D, Sittner A, Piehler J, Dahan M, Coppey M (2018). Non-specific interactions govern cytosolic diffusion of nanosized objects in mammalian cells. Nat Mater 17, 740–746.

Fabry B, Maksym GN, Butler JP, Glogauer M, Navajas D, Fredberg JJ (2001). Scaling the microrheology of living cells. Phys Rev Lett 87, 148102.

Farhadifar R, Baer CF, Valfort A-C, Andersen EC, Müller-Reichert T, Delattre M, Needleman DJ (2015). Scaling, selection, and evolutionary dynamics of the mitotic spindle. Curr Biol 25, 732–740.

Farhadifar R, Yu CH, Fabig G, Wu HY, Stein DB, Rockman M, Müller-Reichert T, Shelley MJ, Needleman DJ (2020). Stoichiometric interactions explain spindle dynamics and scaling across 100 million years of nematode evolution. Elife 9, 1–26.

Garzon-Coral C, Fantana HA, Howard J (2016). A force-generating machinery maintains the spindle at the cell center during mitosis. Science 352, 1124–1127.

Grill SW, Gönczy P, Stelzer EH, Hyman AA (2001). Polarity controls forces governing asymmetric spindle positioning in the *Caenorhabditis elegans* embryo. Nature 409, 630–633.

Grill SW, Howard J, Schäffer E, Stelzer EHK, Hyman AA (2003). The distribution of active force generators controls mitotic spindle position. Science 301, 518–521.

Grill SW, Kruse K, Jülicher F (2005). Theory of mitotic spindle oscillations. Phys Rev Lett 94, 108104.

Hermann GJ, Schroeder LK, Hieb CA, Kershner AM, Rabbitts BM, Fonarev P, Grant BD, Priess JR (2005). Genetic analysis of lysosomal trafficking in *Caenorhabditis elegans*. Mol Biol Cell 16, 3273–3288.

Jain K, Khetan N, Yadav SA, Palani S, Athale CA (2021). Collective dynein transport of the nucleus by pulling on astral microtubules during *Saccharomycescerevisiae* mitosis. Yeast 38, 352–366.

Jiang H (2015). Cell size modulates oscillation, positioning and length of mitotic spindles. Sci Rep 5, 1–10.

Juang JY, Chen PY, Yang DC, Wu SP, Yen A, Hsieh HI (2017). The avian egg exhibits general allometric invariances in mechanical design. Sci Rep 7. doi:10.1038/s41598-017-14552-0.

Khetan N, Athale CA (2016). A Motor-gradient and clustering model of the centripetal motility of MTOCs in meiosis I of mouse oocytes. PLoS Comput Biol 12, e1005102.

Khetan N, Athale CA (2020). Aster swarming by symmetry breaking of cortical dynein transport and coupling kinesins. Soft Matter 16, 8554–8564.

Khodjakov A, La Terra S, Chang F (2004). Laser microsurgery in fission yeast: role of the mitotic spindle midzone in anaphase B. Curr Biol 14, 1330–1340.

Kotak S (2019). Mechanisms of spindle positioning: lessons from worms and mammalian cells. Biomolecules 9, 80.

Kozlowski C, Srayko M, Nedelec F (2007). Cortical microtubule contacts position the spindle in *C. elegans* embryos. Cell 129, 499–510.

Labbé JC, McCarthy EK, Goldstein B (2004). The forces that position a mitotic spindle asymmetrically are tethered until after the time of spindle assembly. J Cell Biol 167, 245–256.

Lanoiselée Y, Moutal N, Grebenkov DS (2018). Diffusion-limited reactions in dynamic heterogeneous media. Nat Commun 9, 4398.

Lynch M (2007). The frailty of adaptive hypotheses for the origins of organismal complexity. Proc Natl Acad Sci USA 104 (Suppl), 8597–8604.

Ma R, Laan L, Dogterom M, Pavin N, Jülicher F (2014). General theory for the mechanics of confined microtubule asters. New J Phys 16, 13018.

Michalet X (2010). Mean square displacement analysis of single-particle trajectories with localization error: Brownian motion in an isotropic medium. Phys Rev E 82, 041914.

Mogilner A, Manhart A (2018). Intracellular fluid mechanics: coupling cytoplasmic flow with active cytoskeletal gel. Annu Rev Fluid Mech 50, 347–370.

Muramatsu N, Minton AP (1988). Tracer diffusion of globular proteins in concentrated protein solutions. Proc Natl Acad Sci USA 85, 2984–2988.

Neves A, Busso C, Gönczy P (2015). Cellular hallmarks reveal restricted aerobic metabolism at thermal limits. Elife 4, e04810.

Pecreaux J, Röper J-C, Kruse K, Jülicher F, Hyman AA, Grill SW, Howard J (2006). Spindle oscillations during asymmetric cell division require a threshold number of active cortical force generators. Curr Biol 16, 2111–2122.

Oegema K, Desai A, Rybina S, Kirkham M, Hyman AA (2001). Functional analysis of kinetochore assembly in *Caenorhabditis elegans*. J Cell Biol 153, 1209–1226.

Quemada D (1977). Rheology of concentrated disperse systems and minimum energy dissipation principle. Rheol Acta 16, 82–94.

Reber S, Goehring NW (2015). Intracellular scaling mechanisms. Cold Spring Harb Perspect Biol 7. doi:10.1101/cshperspect.a019067.

Rieckhoff EM, Berndt F, Elsner M, Golfier S, Decker F, Ishihara K, Brugués J (2020). Spindle scaling is governed by cell boundary regulation of microtubule nucleation. Curr Biol 30, 4973–4983.

Schneider CA, Rasband WS, Eliceiri KW (2012). NIH Image to ImageJ: 25 years of image analysis. Nat Methods 9, 671–675.

Sumi A, Hayes P, D'Angelo A, Colombelli J, Salbreux G, Dierkes K, Solon J (2018). Adherens Junction length during tissue contraction is controlled by the mechanosensitive activity of actomyosin and junctional recycling. Dev Cell 47, 453–463.

Sutradhar S, Yadav V, Sridhar S, Sreekumar L, Bhattacharyya D, Ghosh SK, Paul R, Sanyal K (2015). A comprehensive model to predict mitotic division in budding yeasts. Mol Biol Cell 26, 3954–3965.

Tolić-Nørrelykke IM, Sacconi L, Thon G, Pavone FS (2004). Positioning and elongation of the fission yeast spindle by microtubule-based pushing. Curr Biol 14, 1181–1186.

Tsang WY, Sayles LC, Grad LI, Pilgrim DB, Lemire BD (2001). Mitochondrial respiratory chain deficiency in *Caenorhabditis elegans* results in developmental arrest and increased life span. J Biol Chem 276:32240–32246.

Valfort A-C, Launay C, Sémon M, Delattre M (2018). Evolution of mitotic spindle behavior during the first asymmetric embryonic division of nematodes. PLoS Biol 16, e2005099.